Flat-Plate vs NACA 63A-010 Airfoil Performance for Subsonic, Low-Re Rocketry

Aditya Dinesh

Illinois STEM Society

Naperville, Illinois, USA

adityadinesh09@gmail.com

Abstract

Flat-plate airfoils are widely used in rocketry for their strength and high manufacturability. However, at subsonic speeds, they incur higher drag from early flow separation and turbulence, leading to unfavorable costs and flight efficiency. Laminar airfoils would solve these issues by maintaining a favorable pressure gradient, thereby reducing drag. This project's purpose is to determine efficiency of NACA 63A-010 laminar airfoil over flat-plate airfoils at subsonic speeds. A two-phase procedure was used to compare the two airfoil types at subsonic regimes. Twenty airfoils, including the flat-plate and NACA 63A-010, were tested using XFOIL's 2D airfoil solver. Each airfoil was evaluated for drag, transition behavior, and stability metrics. The second phase of the procedure involved launching identical rockets, each flown twice, with the hexagonal flat-plate and NACA 63A-010 fins. Each carries a BlueRaven altimeter measuring velocity, altitude, and attitude, while an onboard camera assesses stability. Simulations strongly favored the 63A-010 airfoil over the hexagonal flat-plate airfoil, showing a 60-81% reduction in profile drag at Reynolds numbers below 1,100,000, attributable to a longer transition point and lower drag coefficient while also demonstrating improved stability. Flight tests further backed the simulation with an improvement of 10% in peak altitude reached by the rocket using NACA 63A-010 airfoils. Despite 63A-010 airfoil's complex geometry, additive manufacturing enables similar cost and structural performance for both airfoil types. Given its superior performance over hexagonal airfoils, the NACA 63A-010 is a strong candidate for subsonic amateur rocketry and rocket-assisted takeoffs.

Table of Contents

1. Introduction

1.1 Purpose

Aerospace engineering is a broad field that encompasses a range of mechanisms with diverse purposes and applications. However, one commonality between all airborne mechanisms is the airfoil. Its teardrop shape applies to several applications, including wind turbines, boat propellers, car spoilers, and aircraft. Historically, environmental sustainability and fuel waste have been significant issues in the aerospace community; consequently, research on increasing airfoil efficiency is highly sought after.

Regarding space launch systems, conventional rockets use airfoils on fins to enhance stability, and commercial rockets, such as the Saturn V and the Black Brant sounding rocket, use flat-plate airfoils for structural integrity and ease of fabrication. Flat-plate airfoils consist of simple geometries, such as rectangles, hexagons, or diamonds. For the same reason, this type of airfoil is used not only in professional but also in amateur rocketry and Rocket Assisted Take-Off (RATO) systems for Unmanned Aerial Vehicles (UAV) (Nakka, 2024). Flat-plate airfoils have several advantages in the transonic and supersonic regimes, as these speeds require low thickness-to-chord ratios and thickness distributions to minimize wave drag and optimize lift-to-drag ratios. However, these airfoils are avoided for aircraft wings for subsonic, transonic, and supersonic applications, due to their poor aerodynamic performance at low Mach numbers and high angles of attack. As a result, aircraft with these airfoils experience less efficient takeoffs and landings, and worsened lift-off and burnout phases for rockets (Leishman 2022, Chapter 55). Several issues arise from this reduction in performance, including increased fuel wastage due to reduced aircraft efficiency, decreased speed, increased aerodynamic stress on the aircraft, and more turbulent flight due to a shorter chordwise transition length.

When discussing airfoils, the primary classification system is the NACA series, the foundational series of trialed and tested airfoils, which encompasses a wide range of characteristics and applications based on their shape. Within the NACA classifications, the NACA 6-series airfoils are optimized for laminar flow by lengthening the airfoil's transition point. These airfoils are available cambered for aircraft designs and symmetrical for other types of high-speed vehicles, such as rockets.

Current studies on this topic have analyzed airfoils in amateur rocketry fins, such as the NACA 0009 airfoil. This airfoil was tested for drag and lift coefficients in a wind tunnel at both 0 and 90 degrees of AoA at low Mach numbers and subsonic speeds (Robertson, 2025). Despite this, a comparison between specialized airfoils and traditional flat-plate airfoils hasn’t been conducted, real-world rocketry usage hasn’t been applied to analyze airfoils, and other airfoil classifications like the NACA 6-series, which specialize in elongated laminar flow through a delayed transition point, haven’t been applied to rocketry. Additionally, the use of traditional airfoils in amateur rocketry has been undermined by the simplicity of creating flat-plate airfoils, as well as the lack of experimentation and data for rockets flying in subsonic environments due to most commercial rockets traveling at supersonic speeds.

Even though flat-plate airfoils are conventionally used when engineering rockets, the effects of other airfoils were examined at subsonic speeds to test for improved aerodynamic efficiency. The purpose of this investigation is to determine the extent to which laminar flow and other types of airfoils are more suitable than a flat-plate airfoil for rockets flying at subsonic speeds. The comparison will be tested using computational analysis between airfoils in XFOIL, as well as field testing using rocket launches with a flat-plate airfoil and a laminar flow airfoil.

1.2 Hypothesis

The teardrop-shaped 6-series NACA 63A-010 airfoil’s laminar flow characteristics will cause it to outperform a hexagonal flat-plate airfoil at subsonic speeds in model rocketry, achieving lesser drag and greater lift at small angles of attack.

2. Background

2.1 Theoretical Framework

All rockets experience the four main forces of flight: lift, thrust, drag, and weight. These four forces are responsible for rocket characteristics.

Generally, when discussing aerodynamics, which is "the science that deals with the flow of air", optimization of mainly lift and drag is crucial to optimize efficiency (J. D. Anderson, 2016, p. 51). All aircraft experience pressure from air resistance, which is the normal force on an object per unit area exerted by the air molecules striking that surface**.** In a freestream velocity, the lift of an airfoil is determined by a differential in pressure. Per Bernoulli's principle, lift is created by an imbalance of higher pressure at the bottom of an airfoil and lower pressure on the top. The lower-pressure zone causes air to move faster, and the higher-pressure zone causes air to move more slowly (J. D. Anderson, 2017, p. 212). This imbalance in speed and force creates the upwards vector of lift as a result.

Lift is used on rockets as a force to restore the rocket to its intended flight angle when experiencing oscillations, which are unwanted repetitive tilt movements. The equation for the lift force is $L = \frac{1}{2}\rho_\infty V_\infty^2 S C_l$, where L is the force of the lift, ρ_∞ being the density of the air, V_∞ being the speed of the air, which is the freestream velocity, S being the reference area of the aerodynamic surface, as seen in Fig. 1, and C_l being the lift coefficient (J. D. Anderson 2016, pp. 182-184). These variables help determine the amount of lift an aircraft's wings produce. However, the equation for lift shares three variables with the equation for drag: fluid density, velocity, and aerodynamic surface, along with similar variables when finding both the lift and drag coefficients, making it difficult to properly balance out the two forces to make the most efficient airfoil. Drag is the opposing force a solid body experiences when traveling through a fluid, such as air, slowing the object down. The equation for drag is $D = \frac{1}{2}\rho_\infty V_\infty^2 S C_d$, where D is the force of drag, ρ_∞ is the density of the air, V_∞ is the freestream velocity, S is the size of the aerodynamic surface, the reference area, and C_d is the drag coefficient (D. F.

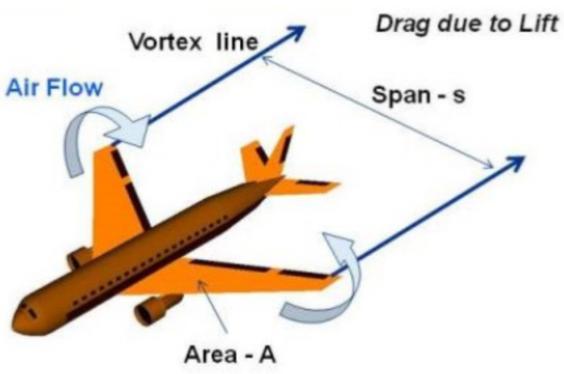

Fig. 1. Diagram how air moves around the wing tip to form vortices (NASA Glenn Research Center, 2022).

Anderson, 2001, p. 185). At subsonic speeds, there are two main types of drag: parasite and induced drag. Induced drag is created when high-pressure air on the bottom of a wing flows up and around the wingtip to the top of the wing, creating a downward flow on the wing, called a downwash. As a result, vortices are created at each wingtip, creating a vector opposing lift as a result. Induced drag can also occur at the trailing edge of a fin. It is a byproduct of lift due to the pressure differential between both sides of the airfoil being proportional in relationship (NASA Glenn Research Center, 2023).

Aside from lift-induced drag, drag caused by the shape of an object is called parasitic drag. Form drag is a type of parasitic drag in which the shape of an object and its resistance to the fluid determine the drag. As air flows around a body, the air closest to the object “sticks to the surface” due to its surface not being smooth. Air tends to get trapped and slows down as it flows over a surface due to the no-slip condition, creating a velocity gradient near the surface of an airfoil, called a boundary layer (J. D. Anderson, 2017, p. 69). Because of the velocity gradient created in the boundary layer, the layers of airflow nearest to the object slow down because of the fluid’s adherent properties. As a result, the difference in speed between the closer and farther layers of airflow creates shear stresses, which are localized forces caused by the boundary layer that are tangential to the curve of an airfoil, causing airflow to shape around an object. This phenomenon is known as the Coanda Effect. However, airflow does not always shape around an object, for when all shear stresses on an airfoil, collectively known as a shear force, reach a value of zero, the boundary layer of airflow separates from the object. Airflow can shape around objects because of viscosity, and its properties affect how much form drag an object has (D. F. Anderson, 2001, pp. 21-23). When air flows around a bluff body, an aerodynamic term for an unstreamlined object, the boundary layer separates from the object due to its sharp angles and thickness. As shown in Fig. 3, this creates a region of vortices behind the object,

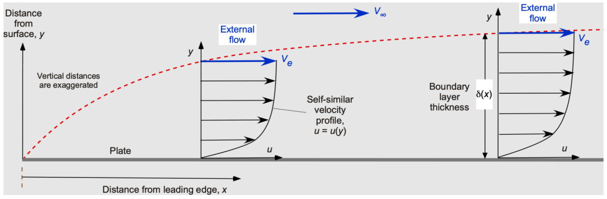

Fig. 2. Diagram of the speed of a fluid adjacent to an object based on the principle of viscosity (Leishmann, 2022).

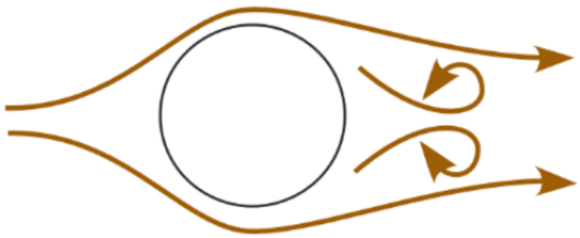

Fig. 3. Illustration of form drag on a sphere and how a wake is created as a result of boundary-layer separation on a bluff body (D. F. Anderson, 2001)

known as a wake, which produces a backward force. Its thickness, determined by how streamlined the object is, affects form drag, so by making parts more streamlined, form drag is reduced because the size of the wake is reduced. (D. F. Anderson, 2001, p. 82). While boundary layer separation is also a factor contributing towards the total makeup of drag, the boundary layer itself is responsible for a type of drag known as skin friction.

Skin friction is caused by the roughness of a surface, with smoother surfaces having less skin friction. Rougher surfaces trap more air and create more resistance, and due to shear forces, the boundary layer expands, producing more drag as a result (Federal Aviation Administration, 2023, pp. 5-6-5-7). Both types of drag apply to all parts of aircraft aside from solely the wings, such as fillets between parts of aircraft, fuselages, and engines. With multiple intersections, the airstreams from different parts of aircrafts intersect, an example being “the intersection of the wing and the fuselage at the wing root.” As a result, vortices, turbulent flows, and other non-laminar currents form, creating a type of drag known as interference drag, which can be reduced by smoothing the joints between connecting parts. (Federal Aviation Administration 2023, p. 5-6).

Drag is important to calculate for aircraft, since this value determines how much fuel the aircraft will require, how fast it can fly, and how long it can be in the air. The equation for drag, $D = \frac{1}{2}\rho_\infty V_\infty^2 S C_d$, where D is the force of drag, ρ_∞ is the density of the air, V_∞ is the freestream velocity, S is the size of the aerodynamic surface, the reference area, and C_d is the drag coefficient (D. F. Anderson, 2001, p. 185). Despite the vast number of drag types, such as profile/parasitic drag and induced drag, to consider when talking about total drag, the formula uses only a few variables. However, the bridge between the two perspectives is the drag coefficient, a dimensionless number required to determine drag. With the use of a drag coefficient, the equation is made using fewer variables, making the main challenge finding the coefficient's value. The drag coefficient accounts for all types of resistance created, such as form drag, induced drag, interference drag, and skin friction. To reduce the drag coefficient through the use of airfoils, objects need to become less susceptible to drag. The main forms of drag to reduce would be form drag and skin friction drag, since interference drag and induced drag are both byproducts of other forces and types of resistance. Form drag can be reduced by streamlining an object. However, streamlining objects requires compromising structural integrity. A reduction in skin-friction drag can solve this issue, and the extent of the reduction depends on the type of flow experienced.

In a viscous environment, air tends to get trapped and slow down within the boundary layer of an object. The layers within the boundary layer pull on each other due to friction, creating stresses known as shear stresses, and these forces along an airfoil collectively make up skin-friction drag (D. F. Anderson, 2001, p. 135). Aside from creating skin-friction drag, the boundary layer determines the type of flow over an airfoil. At the front of an airfoil, the boundary layer is small because the flow is smooth, called laminar flow, as seen in the first section of Fig. 4. As flow continues to move across the airfoil, the boundary layer thickens due to growing shear stresses, which culminate to retard airflow from farther away layers. The enlarged boundary layer also decreases shear stresses due to a reduced velocity gradient. As a result, the boundary layer becomes much more unstable and susceptible to flow separation, so airflow counteracts the reduction in shear stresses by becoming much more chaotic and disturbed. This flow is known as turbulent flow, as seen in the second section of Fig. 4, and due to its uneven nature, the boundary layer is much less susceptible to separating, but it also results in much more skin-friction drag. Finding the thickness of the boundary layer is different for both laminar and turbulent flows due to separate

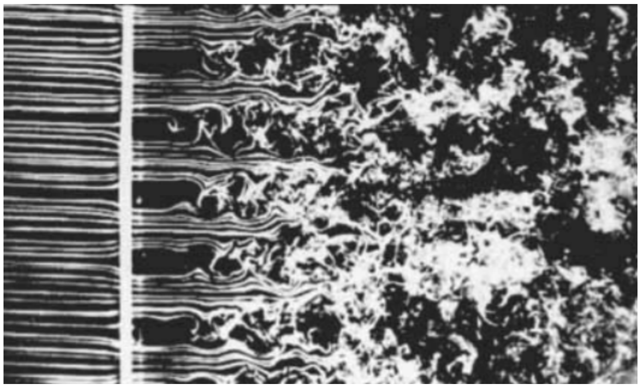

Fig. 4. Photograph of flow turning laminar to turbulent when passing through a plate with holes (D. F. Anderson, 2001).

equations. The equation for a laminar boundary layer is $(5.2x)/\sqrt{Re_x}$, and the equation for a turbulent boundary layer is $(0.37x)/Re_x^{0.2}$, with Re being the Reynolds number and x being the location of the calculated boundary layer for both equations. Due to the boundary-layer growth rate of turbulent flow being rough "$x^{4/5}$", which is "in contrast" to the "slower $x^{1/2}$ variation for a laminar" boundary layer, "turbulent boundary layers grow faster and thicker than laminar boundary layers," (D. F. Anderson, 2001, pp. 141-145). Despite the potential upsides, the "vast majority of practical viscous flows are turbulent," such as those created by "practical airplanes, missiles, ship hulls, etc," because of their stability from increased shear stress. However, in the correct application, the favorable drag reduction characteristics of laminar flow can be used, depending on pressure gradients and the speed of an object.

A pressure gradient is the change in air pressure along the surface of an airfoil in the direction of the airflow. Airfoils are shaped like a teardrop, with the point of maximum thickness being closer to the leading edge, and a tapered down body that continues until the trailing edge. This shape results in a favorable pressure gradient, where pressure decreases when moving in the direction of airflow, and a subsequent adverse pressure gradient, where pressure increases when moving in the direction of airflow. As flow moves from the leading edge to the point of maximum thickness on an airfoil, airflow accelerates due to a favorable pressure gradient. However, when moving from the point of maximum thickness to the trailing edge, airflow encounters an adverse pressure gradient that slows down airflow. Airflow continues to decelerate until, eventually, the fluid particles lose their forward momentum and start travelling in the opposite direction of the airflow, and this is where boundary-layer separation occurs. As a result, a wake is formed, and pressure drag is sharply increased.

Boundary layer separation is more susceptible to laminar flow due to less forward momentum from organized airflow, while turbulent flow creates more forward momentum due to chaos to avoid separation. Flow separation doesn't always occur, for if there's enough forward momentum to overcome the adverse pressure gradient, flow will not separate (Wassgren, 2025, pp. 994-995). Adverse pressure gradients can be affected significantly by varying the angle of attack and freestream velocity. Higher angles of attack create larger pressure between the point of maximum thickness and the trailing edge. This results in far less forward momentum, resulting in an earlier point of flow separation. At high enough angles of attack, pressure drag outweighs the lift generated by the airfoil, resulting in the phenomenon known as stall. For most rockets, fins don't experience dramatic angles of attack, so boundary layer separation tends not to occur. Pressure gradients are also affected by freestream velocity. As freestream velocity increases, both adverse and favorable pressure gradients are amplified, resulting in a moderate impact that encourages flow separation. However, this is dependent on flow compressibility. An incompressible flow has a constant fluid density, while a compressible flow has varying density (J. D. Anderson, 2017, p. 64). In principle, all flows are compressible, but at low enough Mach numbers, flow can be considered incompressible without a detrimental loss of accuracy. A way to determine compressibility is through the use of the critical Mach number, which is the lowest free-stream speed at which any part of an airfoil first reaches Mach 1. If an airfoil's freestream velocity is lower than the critical Mach number, the flow is considered incompressible. For compressible flows, increasing the freestream velocity causes the pressure gradients to become more extreme and even discontinuous, resulting in flow separation being dramatically promoted. In most cases for subsonic rocketry, flows are considered incompressible. Along with the angle of attack not varying drastically in rocketry, the main challenge regarding adverse pressure gradients for this application is balancing it to prevent flow separation while also reducing skin-friction drag. This outcome can be achieved by adjusting the transition point on an airfoil, where laminar and turbulent flows meet.

To determine if a flow is laminar or turbulent, controlling the Reynolds number distribution over an airfoil is crucial. The Reynolds number is a ratio of inertial forces, which resist motion, to viscous forces. It is a dimensionless value, and higher Reynolds numbers indicate more inertial forces and vice versa. The formula for is $Re = (\rho v L)/\mu$, where ρ is density of the fluid, v is velocity of the fluid, L is the linear dimension of the measured body, and μ is dynamic viscosity, which is a measure of the internal friction being created in the boundary layer, calculated using the Sutherland's Formula which calculates changes in absolute temperature (NASA Glenn Research Center, 2024). Along the chord of the object, lower, laminar Reynolds numbers transition into higher, turbulent ones. The point at which this transition happens is known as the transition point, and the corresponding Reynolds' number value at this point is known as the critical Reynolds number. After this point, boundary-layer expansion dramatically increases, as shown in Fig. 5, thereby increasing skin-friction drag.

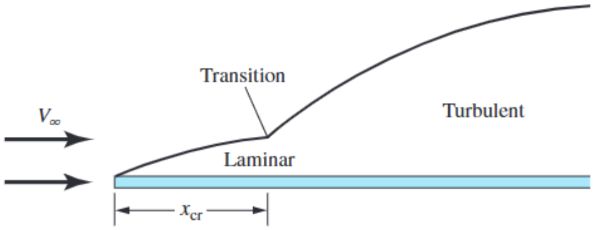

Fig. 5. Illustration of the transition point between laminar and turbulent flow impacting boundary layer expansion (J. D. Anderson, 2017).

This point is crucial to determine skin-friction drag on an object, as the closer the transition point is to the leading edge, the larger area of the airfoil is exposed to turbulent flow, and more skin friction drag (J.D. Anderson, 2017, pp. 385-386).

Transition point was one of the main consideration factors when creating the NACA 6 series of airfoils. NACA airfoils were created and extensively researched in the early 20th century to improve factors such as lift, drag, and stability for wings and fins of aircraft. One specific series of airfoils created by NACA, the 6-series, was created to lengthen the effects of laminar flow and encourage it for a longer portion of the airfoil with a delayed transition point. This was accomplished by delaying the point of maximum thickness farther down the airfoil, which in turn increased the favorable pressure gradient and reduced overall pressure distributions. As a result, skin friction drag was reduced (J.D. Anderson, 2001, pp. 39-40). Many modern forms of laminar flow airfoils were also created, such as the Natural Laminar Flow series of airfoils, designed to specialize in promoting laminar flow in general aviation.

With transition point, Reynolds' number, compressibility, pressure distributions, types of drag, and other variables all taken into account to calculate the drag coefficient of a body, it cannot be calculated using a straightforward equation when solving for total drag. As a result,

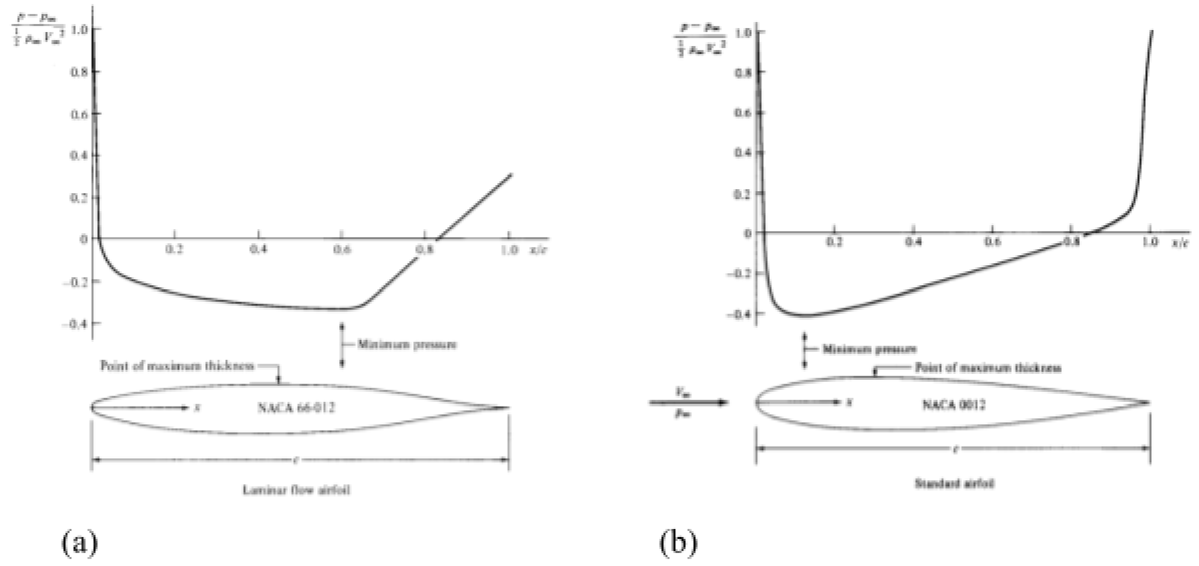

(a) (b)

Fig. 6 Illustrations and graphs of pressure distributions over the NACA 0012 (a) and NACA 66-012 (b) airfoils in determining the extent of the laminar flow region (J. D. Anderson, 2016).

two-dimensional and three-dimensional computer simulation methods such as Computational Fluid Dynamics (CFD), panel method solvers, and Vortex Lattice Method (VLM) are required to solve it. However, even work using computers to calculate this value is not exact, since simplifying assumptions are required to make the math tractable. As a result, along with most theory-based simulations, experimental testing through wind tunnel trials and sensor-based flight evaluation is done as well (J. D. Anderson, 2016, pp. 185-186). For most airfoil analysis, an airfoil is analyzed as an infinite wing, where the airfoil's thickness is infinite, resulting in only two quantifiable dimensions of flow to analyze. This is called two-dimensional analysis, which is far simpler to calculate drag compared to traditional analysis with finite wing-lengths, called three-dimensional analysis. Both methods of analysis differ significantly in the value of the drag coefficient, as three-dimensional analysis accounts for induced drag in addition to all forms of parasite drag due to wingtip-vortex generation. (J. D. Anderson, 2016, pp. 192-194). Despite both methods producing different values for the drag coefficient, the percent difference between the two types of airfoils in both infinite and finite analysis will be very similar due to induced drag being determined by wingtips rather than airfoils. As a result, two-dimensional analysis is widely used for practical analysis when comparing airfoil types for certain aircraft.

2.2 Thematic Literature Review

While the existing theory established regards fundamental flight mechanics, the effects of laminar and turbulent flow on airfoils, different types of drag and boundary layer separation in viscous flows at lower Reynold's numbers, and primary testing methodology to find aerodynamic coefficients, contemporary research reveals how this theory is applied across three principle themes to help solidify the purpose of comparing flat-plate and laminar flow airfoils at low Reynold's numbers. These three themes include real-world application of laminar flow airfoils, performance of different fin cross-sections, including airfoils, in rocketry, and improving performance in RATO systems and amateur rocketry. This section will review each of the three themes using eight studies to compare purposes and address research gaps, and then provide a framework to organize the different concepts, gaps, and relationships provided.

The opening theme questions the real-world application of laminar flow airfoils. Most laminar flow airfoils, especially those within the NACA 6-series, haven't been tested in real world application. The creators of the NACA 6-series, NACA itself, tested their symmetrical 6-series airfoils at low speed, high Reynolds' numbers, with varying angles of attack and thicknesses of six, eight, ten, and twelve percent of the chord length, using the "Langley low-turbulence pressure" wind tunnel. Another variable implemented into the test was the intentional roughening of the leading edge to determine how drastic an effect it would have on airfoil performance. These tests were to determine drag, lift, and pitching moments. Overall, drag increased proportionally with thickness and increased with rougher leading edges (Wilson & Horton, 1953). Contemporary testing of laminar flow airfoils involves computational analysis through methods such as CFD and XFOIL. Using CFD, a study tested the effects of different sweep angles for the NACA 65(3)-218 6-series airfoil at Mach numbers between 0.6 and 1.2, concluding that the 35° angle was the most efficient. The study specifically used the NACA 6-series due to their high performance in ideal situations (Selvaraj & Paul, 2014). Finally, similar to the implementation of surface roughness for analysis, a study from Kuwait University conducted experimentation to analyze differences in drag, lift, pressure distribution, and turbulence on a NACA 0012 airfoil with three distinct surface roughnesses: smooth, 80 microns, and 120 microns. Tests were conducted using a wind tunnel at low Reynolds numbers and angles of attack of 0° and 15°, with results exhibiting a high performance difference between each surface roughness (Abdel-Rahman & Chakron, 1997). These three studies analyze laminar flow airfoils using various computational methods, such as CFD, and experimental methods like wind-tunnel testing. Together, the studies conclude and mention that while laminar flow airfoils display favorable pressure distributions and drag characteristics in subsonic, incompressible, and viscous environments, their performance drastically worsens with a rougher surface finish. Despite these conclusions, actual application and testing of these airfoils on aircraft such as rockets, in realistic, non-ideal situations, hasn't been conducted, especially as a comparative analysis between computational and experimental methods. Wind-tunnel testing from papers by Wilson and Horton, as well as Abdel-Rahman and Chakron, has helped address this gap, but these tests were conducted in an ideal and constant environment, drastically different from real-world applications.

The comparison between different airfoils and cross sections in rocketry is a topic that hasn't been addressed. Richard Nakka's annotated bibliography showcased all the different ways fins of rockets could be modified and the impact they would showcase. It is mentioned that airfoils for rocket fins don't impact performance drastically for smaller rockets, but larger rockets with thicker fins may be beneficial (NACA, 1945). These benefits were seen on Nakka's launch of the Frostfire 3 rocket. It was also observed for subsequent launches that the benefits of airfoiled fins were only seen before compressibility effects increased prior to transonic regimes, due to dynamic instability occurring at those speeds. According to Nakka's observations and flight experience, regions past this most commonly utilize double-wedge and modified double-wedge cross-sections to minimize flow separation (Nakka, 2024). Worcester Polytechnic Institute published a paper regarding the process of building a specialized rocket with the overall intent being to launch and fly a rocket to 460m using systems such as actively controlled canard fins, a CO2 pressurization system for parachute deployment, and a retromotor to slow descent, while also improving efficiency when feasible. Regarding efficiency improvements through the reduction of drag, nosecone, canard, and fin shape were all extensively considered. Each system was considered after listing several different options and determining the best fit for their project's subsonic application. However, the use of airfoiled fins was briefly mentioned, explaining that they can be used on specialized rockets, with most using flat-plate airfoils regardless of Mach number. Furthermore, their rocket utilized a flat plate airfoil despite traveling at subsonic conditions (Bowers et al., 2022). As mentioned, airfoiled fins were used for specialized applications such as rotation-inducing fins. The University of Akron utilized the NACA 2412 cambered airfoil to induce roll onto the rocket to increase stability through the use of rotation. The effects of this airfoil were examined through wind tunnel testing of the entire rocket and CFD analysis on the entire apparatus, as well as the fin individually (Saylor et al., 2016). All three studies deduced that airfoil usage at subsonic speeds can be conducted, but hasn't been extensively implemented and analyzed. The lack of papers regarding the comparison of airfoils in rocketry further supports the lack of experimentation, and of the current experimentation, most papers conducted research for stability applications regarding rotation-inducing airfoils, as mentioned in both Richard Nakka's experiments regarding rocket design, Worcester Polytechnic Institute's paper on the construction of their subsonic rocket, as well as the University of Akron's experimentation on this phenomenon. As a result, comparison regarding drag behavior between airfoils hasn't been conducted, especially with the opportunity for performance improvement at subsonic speeds.

Performance improvement of both Rocket Assisted Takeoff (RATO) systems and amateur rockets is highly sought after and can be accomplished through many means, airfoil design being a venue that has been explored minimally. The commercial viability of a specific RATO design developed by Oklahoma State University was proposed as a way to launch UAVs into the air without modifying the UAV itself. The main purpose of the system was to launch the UAV to around Mach 0.2 at a 10° flight angle, with an emphasis on reusability of the RATO system. Overall, the mission goals for the UAV were accomplished using this detachable RATO design. One of the main issues with the RATO system, listed as a point to address if used commercially, was the reduced stability resulting from the center of gravity being shifted backward (Greif et al., 2023). Similar to improvements in RATO systems, the ZHAW School of Engineering tested drag and stability between three different types of fin shapes at subsonic and transonic environments using CFD, to eventually be able to use them on their Helvetia rocket. The group tested the Helvetia, Piccard, and swept parallelogram fins at transonic speeds with an angle of attack range between 0° and 30°. The overall goal of the project was to maximize efficiency on the Helvetia rocket, and one of the main reasons why the swept parallelogram fin was the best performing regarding both characteristics was due to the delayed transition point provided by the swept nature of the fin (Schoch, 2023). Both studies focused on the aerodynamic optimization of their respective systems, and that was accomplished using systems such as detachable designs and fin-shape optimization, which decreased drag, increased stability, and reduced fuel consumption. Despite these beneficial results, Gref's experimentation faced stability-related challenges due to RATO systems shifting the center of gravity. Adding fins to the RATO system would solve this issue by shifting the center of pressure back, but this results in an increase of drag, deviating from the main goal of reaching a high enough target velocity while minimally using fuel, but through proper airfoil comparison and analysis, the right type of airfoil can be utilized to minimize drag while providing stability for this system. Schoch's experiment on fin design optimization concluded that laminar flow effects from testing were a larger factor in drag reduction than their initial hypothesis, which centered on a larger surface area being the favorable factor. Using these insights into laminar flow, other system modifications, such as airfoils, could have been implemented to promote this phenomenon, but developments in this field have been limited, especially in subsonic speeds. Overall, the performance improvement field for RATO systems and amateur rockets has hardly addressed airfoil optimization, especially with the lack of data and information regarding it.

Across all three themes, a consistent pattern emerges: while airfoil usage and laminar flow airfoils provide beneficial drag and stability characteristics to RATO systems, rockets, and in simulation, their actual use case in rocketry, especially in subsonic environments, has not been explored comprehensively, data collection and comparison is sparse, and most testing is conducted simulationally or through wind tunnels rather than actual field testing. Together, these gaps prevent a mission-level understanding of whether the usage of airfoils in rocketry and RATO systems, specifically laminar airfoils, provides a substantial increase in performance compared to traditional cross-sections used in rocket fins, like the flat-plate airfoil. The following sections will address this overarching gap with a comparative analysis of different airfoils, specifically between the NACA 63A-010 and hexagonal flat-plate airfoils, to test the extent to which laminar flow effects improve performance.

3. Materials and Methods

3.1 Overview

To test the difference in efficiency and cost between hexagonal flat-plate airfoils and the 63A-010 at subsonic speeds, a two-part procedure was implemented, utilizing simulation and experimental methods. The first part of the procedure required testing a batch of 23 distinct airfoils, including the NACA 63A-010 laminar airfoil and the hexagonal flat-plate airfoil, to determine how different airfoil characteristics impact performance. Three main methods of simulation were considered for simulating this batch of airfoils. Reynolds Average Navier-Stokes (RANS) CFD was the first option, which works by solving the Navier-Stokes equations to solve for the motion of a fluid moving over an object, and it utilizes a turbulence model to average out flow in the turbulent section of an object. RANS CFD was useful to calculate all aerodynamic coefficients and pressure distributions in three dimensions, allowing for calculations such as interference drag to become possible. This method can encounter issues with high-separation flows and computing in transitional regimes. The second option was

Large Eddy Simulation (LES) CFD Dynamics, which works the same way as RANS CFD while also calculating vortex and eddy formation within the turbulent layer rather than using an average. LES encounters issues even with the slightest issues with the background and mesh setup. The final option was XFOIL's 2D Viscous-Inviscid Interaction Simulator. Despite its lack of three-dimensional capabilities, XFOIL uses a global Newton method to calculate boundary layer and external airflow simultaneously to get two-dimensional aerodynamic and frictional coefficients of an airfoil. All three methods were viable options for simulating the batch of airfoils; therefore, Table 1, a design matrix, was created to determine which method would be the most practical to use. Before the creation of the decision matrix, the critical Mach number was calculated to determine whether compressibility would be a factor, as both CFD methods use much more accurate compressibility-correction methods than XFOIL's Karman-Tsien correction (Drela, 1989, pp. 1-12). Using the formula, the Mach number was 0.7664 for the NACA 63A-010 airfoil, and 0.7275 for the hexagonal flat-plate airfoil, and with the maximum speed of the aircraft being at least 40% less than the critical Mach number, the flow is considered incompressible. As a result, the feature utility category in the decision matrix was decreased for CFD without the need for compressibility corrections, and accuracy for

Table 1. Criteria were weighted to prioritize simulation method proficiency while considering practicality. XFOIL was the chosen simulation method due to its high accuracy at subsonic, low Reynolds number, making it more compatible due to an incompressible environment. Despite both CFD methods having high accuracies, the tradeoff was a longer setup time due to individual 3D models and mesh modelling for each airfoil, as well as domain creation. XFOIL's lack of 3D capabilities was deemed acceptable due to the rocket's subsonic regime and constant fin measurements, minimizing the need for 3D CFD features. Finally, both CFD forms required much longer calculation times and more demanding hardware, making it not widely accessible for the repeatability of the procedure.

	XFOIL	RANS CFD	LES CFD
Accuracy (30%)	8	9.5	**10**
Setup Time (20%)	**9**	4	2
Calculation Speed (15%)	**10**	5	2
3D Capabilities (15%)	1	9	**10**
Compatible Hardware (10%)	**10**	5	1
Feature Utility (10%)	**9**	6	3
Total	**7.75**	6.85	5.6

XFOIL was increased due to it being an incompressible flow. Based on these six weighted criteria, XFOIL was selected as the simulation method for its high accuracy in subsonic, low-Reynolds-number flows and faster setup times and computational speeds. Using XFOIL, the batch of 23 airfoils was narrowed down to seven once constants were implemented. These airfoils would then be tested for four main characteristics: drag, transition point, drag sensitivity, and restoration force, and all data points for each airfoil would be collected and exported into Excel to polish and create graphs.

The second part of the procedure involved launching a rocket twice, the first time with NACA 63A-010 airfoils, and the second time with hexagonal flat-plate airfoils. Before building any rockets, simulations of flight were conducted on OpenRocket to account for stability margins, part sizing, motor selection, recovery method selection, and weight. After simulations, the rocket was fully created. For both launches, the rocket was equipped with an onboard camera for qualitative stability measurements, two altimeters with barometers to measure atmospheric pressure and altitude, gyroscopes to keep track of attitude, and accelerometers for velocity and acceleration readings. Data from both flights was compared with each other as well as simulation results from XFOIL to see what external factors in the real world weren't simulated in XFOIL. To ensure utmost safety, standards from the National Association of Rocketry (NAR), the Federal Aviation Administration (FAA), and AeroTech were all followed to ensure safety for all launches.

3.2 XFOIL and OpenRocket Simulation Procedure

3.2.1 Variables

Before running simulations in XFOIL's direct airfoil analysis, background variables and constants had to be correctly set to configure the project environment. Assumptions such as the infinite airfoil model, as well as non-turbulent free streams, were made by XFOIL. The main ranges and variables being held were the angle of attack, Reynolds numbers, and Mach numbers, with both the Reynolds number, determined by the Mach number, and the angle of attack ranges being the independent variables of the simulation. Angle of attack ranges were determined based on how much the rockets face when flying. This angle is very low and close to zero most of the time during a rocket's flight, so keeping the angle of attack range between -7 and 7 degrees allowed for a large enough range to account for most tilt experienced by a rocket. Mach numbers were calculated based on the OpenRocket simulation. By modelling the rocket's weight distribution, fin area, nosecone, type of motor, and all other rocket components, the velocity/Mach number was calculated using net force at 0.1-second intervals. Acceleration for the net force calculation was equated using the $a = \frac{(F_{thrust} - F_{drag} - F_{gravity})}{m}$ equation. This method, known as the Runge-Kutta method, has been further improved to find even more accurate velocities using numerical integration (Niskanen, 2009, pp. 65-67). Finally, Reynold's numbers were calculated using environmental constants and flight variables. Five intervals at intervals of Mach 0.1 were used between Mach 0.1 and 0.5. With the Reynolds' number formula, $Re = \frac{\rho v L}{\mu}$, requiring constants for density and temperature for both the equation and the dynamic viscosity from Sutherland's formula, OpenRocket was utilized to calculate the altitude at each Mach number interval to find these environmental constants. Due to it being a universalized baseline in rocketry to determine air characteristics based on altitude, the 1976 US Standard Atmospheric Analysis was used to calculate both the density and temperature at each Mach interval (NASA, 1976). Once the temperature was calculated, the dynamic viscosity had to be calculated using Sutherland's formula, $\mu = \mu_0 \frac{T_0 + C}{T + C} (\frac{T}{T_0})^{\frac{3}{2}}$ where μ is the dynamic viscosity, μ_0 is the reference viscosity, C is Sutherland's constant, T is the temperature, and T_0 is the reference temperature. Reference viscosity, the Sutherland's constant, and reference temperature are all constant for air, making the only variable left to find the temperature at each interval of altitude (NASA, 2009). These three constants are listed in Table 2.

Table 2. Constants for Sutherland's formula for air.

	Value for Air
Reference Viscosity (μ_0)	$1.716 \cdot 10^5$
Reference Temperature (T_0)	273K
Sutherland's constant (C)	110.4

After finding the dynamic viscosity, as well as the air density at each interval, the final variable left was the linear dimension of the airfoil. With the airfoil's chord length not being a constant value due to the design of the fin for the actual rocket, the mean aerodynamic chord length (MAC) was used instead, using the equation $MAC = \frac{2}{3}C_R\frac{1+\lambda+\lambda^2}{1+\lambda}$, where C_R is the root chord and λ is the taper ratio of the root chord to the tip chord. After all three ranges and variables were calculated, the final constant, which is the Ncrit value, was set at 9 for all airfoil analyses. The Ncrit value determines how turbulent the freestream velocity is, and it was set at 9 because it is the default value for clean conditions. Four main graphs were plotted over both Reynolds' number and the angle of attack range to evaluate airfoil performance. The first one was the drag coefficient, the dependent variable, based on Reynolds' number, held at a constant 0-degree angle of attack. Finding drag based on Reynolds number helped determine how much drag would be produced in a flight and which airfoil would be the most drag-efficient. The second graph measured the transition point, the dependent variable, over reynold's number to determine how much of the surface of an airfoil would be laminar, helping to determine skin friction drag during flight. The third graph measured drag, the dependent variable, over a -7 to 7 degree angle of attack range at each Reynolds number, helping to determine how sensitive the airfoil is to angle of attack variations. This input is critical for stability purposes as well, for an airfoil with high sensitivity to changes in angle of attack may experience an unstable and unsafe flight. The final graph measured lift, the dependent variable, over the same angle of attack range at each Reynolds number, which helped determine the restoration force of each airfoil and how quickly it would be able to recover to an angle of attack of 0. These four graphs are crucial in determining the most important airfoil as they evaluate not only its performance, but where it derives its performance benefits from, and how well it responds to minor deviations in flight.

3.22 Procedure

Before conducting XFOIL testing, an OpenRocket simulation was created to find Reynolds' number intervals for the simulation. The OpenRocket simulation, shown in Fig. 7, was a detailed model of the rocket created for this project's flight testing, and it contained

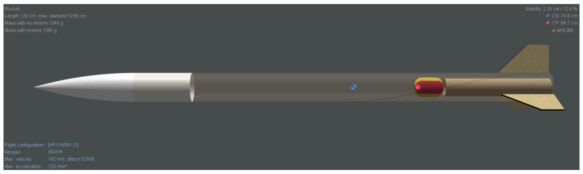

Rocket
Length 120 cm, max. diameter 6.68 cm
Mass with no motors 1040 g
Mass with motors 1396 g

Stability: 2.24 cal / 12.4 %
CG: 74.8 cm
CP: 89.7 cm
at M=0.300

Flight configuration: [HP-I140W-12]
Apogee: 3543 ft
Max. velocity: 192 m/s (Mach 0.569)
Max. acceleration: 120 m/s²

Fig. 7. Simulation of the launched rocket in OpenRocket.

components such as a fiberglass bodytube, a nosecone, fins, an I140W rocket motor, a motor mount, centering rings, kevlar shock chord, a parachute, and an 80g weight component inside the nosecone to account for electronics. The parachute and shock chord were modelled to sit all the way down on the rocket on top of the motor mount due to gravity pushing both components all the way down when a flight begins. The fins were shaped as trapezoidal clipped delta fins. These fin dimensions were determined after the creation of the entire rocket body to determine an adequate size to keep the rocket stable enough. The dimensions and quantity of all these parts is listed in Table 3. Stability margins should be at least 1.5 caliber, which is the diameter length, between the center of pressure and center of mass, and/or 8-18% the length of the entire rocket distance between the two points. The rocket's simulated weight is 1.4kg, and its length is 1.2m.

Using the simulation, the rocket was projected to fly at a max speed of Mach 0.568 to 1078m. Along with a graph for the altitude at each 0.1 Mach number interval (Fig. 8), the data provided from OpenRocket helped to start testing in XFLR5's XFOIL airfoil analysis.

Table 3. Dimensions for each component used for creating the TwinFins OpenRocket simulation. These values were later adjusted for the actual creation of TwinFins.

	Dimensions	Quantity
Fiberglass Bodytube	67 mm diameter, 76.2 cm length	1
Nosecone	24 cm length	1
Fins	55.25 cm^2 area	3
Kevlar Shock Chord	4.5 m long, 3.2 mm diameter	1
Parachute	45 mm diameter	1
Motor mount	38 mm diameter, 24.4 cm length	1

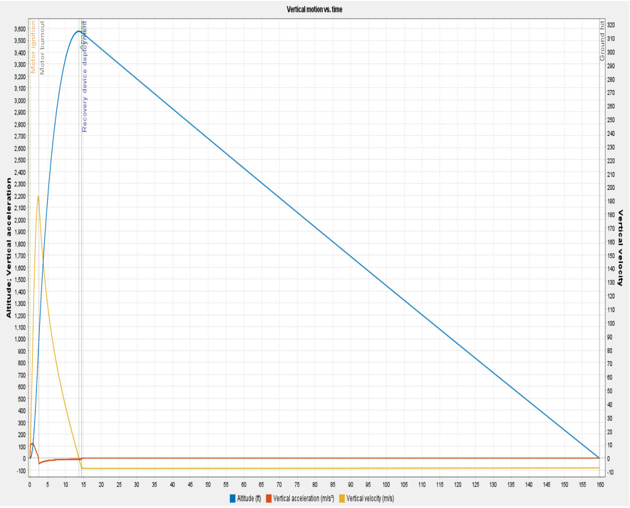

Fig. 8. Simulated altitude vs time, vertical acceleration vs time, and vertical velocity vs time graphs in OpenRocket, along with flight events such as burnout, parachute deployment, and apogee.

Initially, a batch of 23 airfoils was chosen. This batch had airfoils with relatively distinct characteristics, such as varying amounts of camber, thicknesses, thickness distributions, symmetries, and classification systems. All airfoils were initially tested to determine how these characteristics impact the performance of an airfoil using the four graphs, and what constants needed to be set in place before testing the focused group of airfoils. Once complete, a group of seven airfoils was tested, including the NACA 63A-010, NACA 0010, hexagonal flat-plate, Selig SD8020-010-88, Prandtl D-tip (9.6% thickness), WORTMANN FX 76-100, and Quabeck HQ 0/10, and all of these airfoils are shown in Fig. 9. These airfoils are from different classification systems and feature different pressure gradients to manipulate variables such as flow separation; however, all of them are set at a constant maximum thickness of 10% and are symmetrical airfoils featuring no camber. These two constants help decrease variation from other variables in testing and emphasize the focus on how pressure gradients and flow transition affect drag. After simulating all seven airfoils, the polars were exported to Excel to sort data, create graphs,

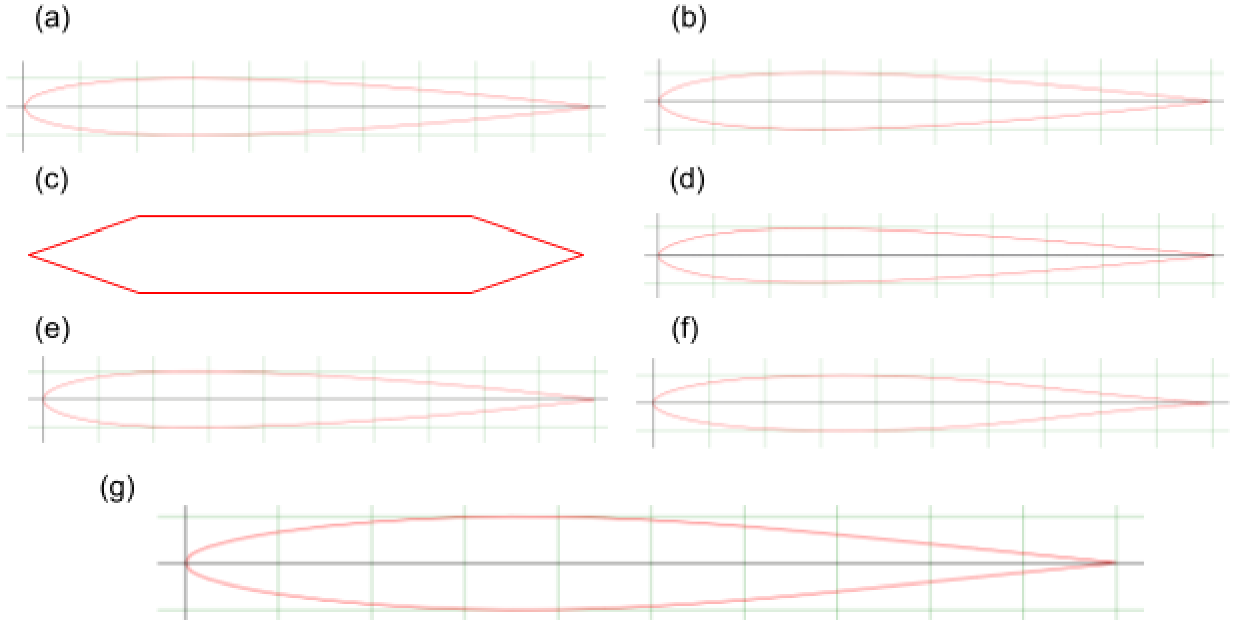

Fig. 9. Geometric profiles of the 7 airfoils analyzed in XFOIL: (a) NACA 0010, (b) SD8020-010-88, (c) Hexagonal Flat-Plate, (d) Prandtl D-Tip, (e) WORTMANN FX 76-100, (f) Quabeck HQ 0/10.

and determine which airfoil was the best for usage. The best airfoil was determined based on consistency of results across all four graphs, all five Reynolds' number intervals, and the entire angle of attack range, as well as performance qualities from each graph.

3.3 Rocket Launches Experimental Procedure

3.31 Variables

The second phase of the procedure had one independent variable, which was the airfoil type for all three fins for each rocket launch. The first fincan had hexagonal flat-plate airfoil fins shaped as clipped-delta fins. The second fincan used the NACA 63A-010 laminar flow airfoils, shaped the same way. Both fincans had the same properties aside from the airfoil shape. These two different airfoils were compared using a list of dependent variables, calculated using an onboard BlueRaven altimeter. Variables directly output from the two flights used as dependent variables were altitude, maximum velocity, maximum acceleration, peak dynamic pressure/max q, velocity at burnout, and maximum tilt angle. Using these variables, the OpenRocket simulation discussed in 3.2, as well as constants based on the motor and rocket specifications, four more dependent variables were used to compare flights.

The first variable is the altitude per impulse, which determines the total altitude achieved per unit of energy, to indicate how performance-efficient the rocket is. This metric is derived from the equation $\frac{h_{max}}{I_{total}}$, where h_{max} is peak altitude, and I_{total} is the total impulse. RMS tilt was the second derived dependent variable, calculating the root mean square, or the typical magnitude, of tilt experienced by a rocket during flight. This was useful for calculating how stable each airfoil was during flight. The equation is

$RMS\ Tilt\ = \sqrt{\frac{1}{N}\sum_{i=1}^{N} \theta_i^{\ 2}}$, where N is the number of angle of attack samples gathered during flight, and θ_i is the tilt angle at each sample, and the equation is a summation due to it utilizing multiple values of tilt rather than 1. The lower the value, the more stable the flight, but the higher the value, the more oscillations are experienced during flight, resulting in a less stable flight. The third variable is the effective drag coefficient of the flight, which is the drag coefficient calculated during flight.

Calculating this would be crucial in comparison between XFOIL and the rocket launches, and between both flights to see the difference in drag and whether laminar flow had an impact on the rocket's flight. The equation for this is $C_d^{eff} =- \frac{2}{p(h)v^2A}(m\frac{dv}{dt} + mg)$, where p(h) is the air density at the specified altitude, A is the cross-sectional area of the rocket, v is the filtered velocity, m is the mass of the rocket, $\frac{dv}{dt}$, is the filtered acceleration, and g is the force of gravity, which is approximately -9.8m/s^2. The coefficient was computed at each time sample during the coast phase of each flight, and measurements for velocity and altitude were taken at a sampling rate of 50Hz using a BlueRaven altimeter. Before using the equation, the velocity was filtered through a Savitsky-Golay filter to smooth out sensor noise and vibrations during flight while preserving the actual flight dynamics. The filtered velocity values were used for both the effective drag coefficient and the final dependent variable, which was the velocity decay rate at burnout. This value determined the negative acceleration during the coast phase of the flight. The equation for this is $a_{total} =- (g + (\frac{\rho \cdot v^2 \cdot c_d \cdot A}{2m}))$, where density was found using the 1976 US Standard Atmosphere, and the other variables, such as mass, velocity, cross-sectional area, and drag coefficient, were found using OpenRocket, flight data, real-world measurements, and other equations, such as the effective drag coefficient equation.

Before and on launch day, several constants were held in place to ensure accuracy when comparing both launches. Both rockets were launched on the same day, 1 hour apart, with both launches having wind speeds of 3km/h and 2.4km/h, respectively, coming from the east, humidity at 48% for the first launch and 51% for the second, pressure readings at 102.7kPa for both launches, and temperatures at -6° Celsius. Both rocket motors were I140W motors with a constant 12-second ejection charge, and each rocket launch was on the same rocket with different fin cans that weighed the same weight in grams.

3.32 Procedure

Before manufacturing the rocket, hereby referred to as TwinFins, both the nosecone and the two fincans were 3D modelled in Fusion 360, along with other supplementary models for both components. Fig. 10 and Fig. 11 are pictures of the modelled components. The nosecone of Twin Fins featured a 24cm long tangent-ogive shaped shell, and a 13.1cm long shoulder to insert into the body tube. The shoulder of the nosecone was modelled with a gap to insert the push-in avionics bay, which housed all of the electronics for the rocket. The shoulder also featured vent holes and a camera hole to ensure accurate altimeter readings and visible onboard camera footage. The two fincans of TwinFins featured three fins, a bodytube section connecting all three, and a hole right through the middle of the rocket for the motor mount. The bottom of the rocket featured a hole for the motor mount and a depression for the motor retainer. The retainer, as well as the bottom of the fincan, featured two holes for a screw to go through. Inside the fincans on top of the two holes were hexagonal enclosures for fitting hexagonal lock nuts to be glued in place when printing. This allows the screws to have proper threads to screw the screws into and connect the retainer and fincan while preventing the motor from coming loose. The top of both fincans featured a depression with 64mm ISO Metric profile threads, and two holes to tie and glue the shock chord around as a strong attachment point. The threads provided the ability to screw on the fincan into the body tube of the rocket, allowing for the ability to swap out fincans to test both flights on the same rocket. To attach the fincans, a threaded coupler was modelled to be glued on the bottom of the body tube to allow for the fincans to be screwed onto the body tube. The final components were two 1010 rail guides for 67cm body tubes, allowing for the rocket to be launched off this launch rail.

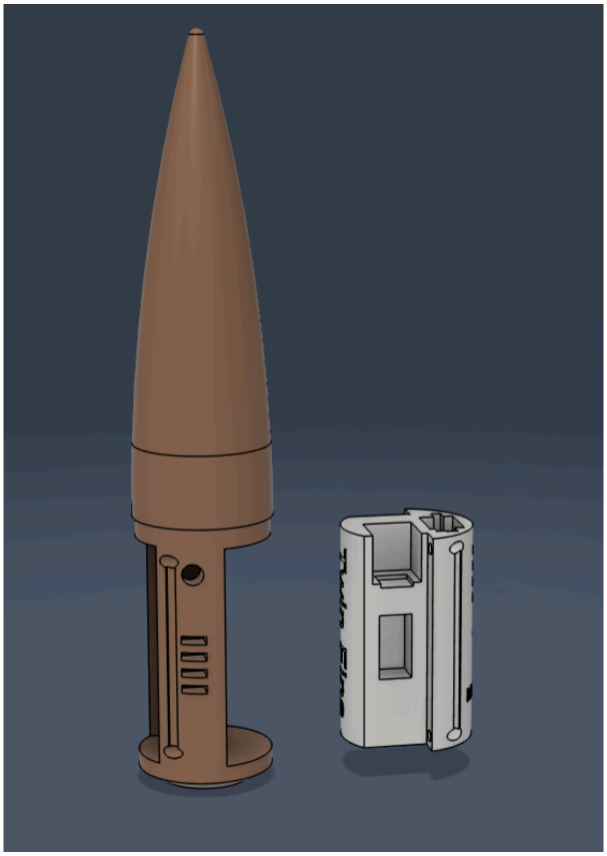

Fig. 10. 3D model of the TwinFins nosecone and the push-block avionics bay.

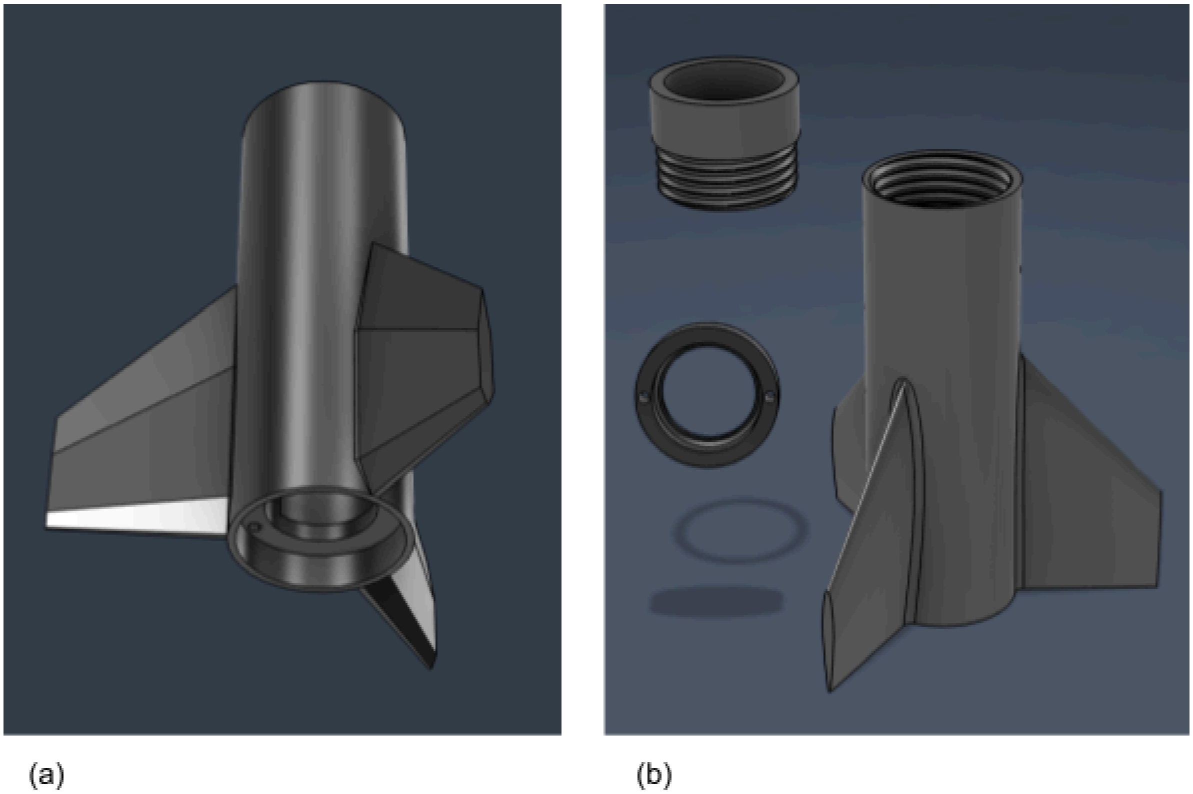

Fig. 11. 3D models of the TwinFins hexagonal flat-plate airfoil fincan (a), screw-on motor retainer, threaded coupler, and NACA 63A-010 airfoil fincan (b).

All items were printed using gray PETG filament for high strength and heat resistance using the Bambu Lab A1 3D printer. Due to the nosecone's overall height exceeding the maximum print height of the printer, it was split up into two prints: the shoulder and bottom of the nosecone, and the top of the nosecone. Printing all 8 components took a total of 46 hours 18 minutes and 1044.53 grams of filament including supports, with the 63A-010 fincan taking 11 hours 58 minutes and 289.38g, the hexagonal flat-plate fincan taking 12 hours and 286g, the bottom of the nosecone taking 7 hours 18 minutes and 150.78g, the top of the nosecone taking 5 hours and 42 minutes and 134.5g, the avionics bay taking 5 hours 20 minutes and 113.14g, the coupler taking 2 hours and 48 minutes and 55.85g, the two rail guides taking 34 minutes and 4grams of filament combined, and the retainer taking 38 minutes and 10.88g of filament. All parts were printed with tree support generation to save filament and support overhangs properly, and brims to ensure parts do not come loose when printing. Before each print, the print plate was cleaned thoroughly with water and dish soap to ensure proper bed adhesion. Both fincan prints were stopped right after the hexagonal enclosures to hold the lock nuts had been printed, as the lock nuts were glued using superglue inside the two enclosures.

After printing, the rocket was assembled. A fiberglass body tube was used instead of cardboard due to its enhanced strength and pressure properties, as well as its ability not to be structurally impacted by water when landing in snow. Three holes were drilled into this body tube, two for the altimeters so that they could receive proper barometer readings, and one for the onboard camera. A 6.35mm machined eyebolt was used to attach a 6.35mm quick link, which held both the parachute and the shock chord. This eyebolt was attached to the bottom of the nosecone after drilling a hole and mounting it inside. The Kevlar shock chord had a thickness of 3.175mm, and two of these were used to attach to each fincan individually. Finally, a cardboard motor mount of 38.6mm in diameter was attached and glued to each fincan. Due to surface roughness and layer lines from 3D printing both fin cans, as seen in Fig. 12a, the fins on each fin can was wet-sanded using 220 grit sandpaper for 15 minutes, 400 grit sandpaper for 15 minutes, and 800 grit sandpaper for 20 minutes to smooth out the airfoil surfaces, with the final product shown in Fig. 12b. Due to the fiberglass body tube's surface roughness, it was spray-painted with a single coat after assembly. A visual of TwinFins is seen in Fig. 13.

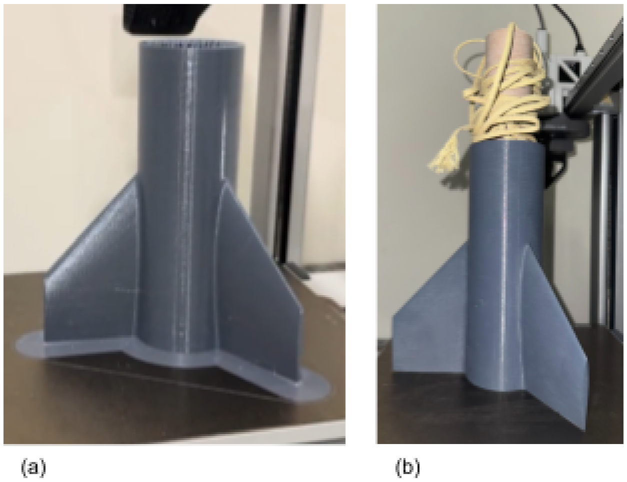

Fig. 12. The NACA 63A-010 fincan before and after sanding.

Before launching each rocket, electronics, parachutes, and motors were prepared. The avionics bay housed two altimeters for redundancy. The first altimeter was the EasyMini, a compact and minimalistic altimeter featuring a barometric sensor, weighing 6.5g, and requiring a single-cell Lithium Polymer (LiPo) battery (AltusMetrum, 2024). The second altimeter was a BlueRaven altimeter, housing sensors such as a

Fig. 13. Photograph of the rocket, TwinFins, leaving the launch pad.

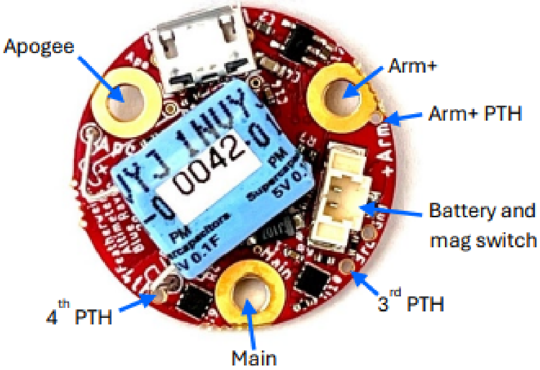

Fig. 14. Photograph of the BlueRaven altimeter and its identified components.

500 Hz 3-axis High-Range Accelerometer, 500 Hz 3-axis High-Resolution Accelerometer, 500 Hz 3-axis gyroscope angular rates, a 50 Hz barometer, and a 50 Hz temperature sensor. This altimeter can use a single-cell LiPo battery, and it weighs 6.8g. The altimeter has Bluetooth capabilities to provide realtime sensor readings and continuity on the launchpad (Featherweight, 2025). Fig. 14 is a picture of the BlueRaven altimeter. Aside from the two altimeters, the avionics bay also houses a switch for the EasyMini altimeter, a noise beacon to emit loud sounds for recovery, and an onboard camera recording in 1080p. Each motor was prepared by adding black powder for the ejection charge, and secured using the retainer on the fincan. The shock cord and the parachute from the fincan were tied to the nosecone, and a parachute protector was tied to the shock cord to prevent any damage to the parachute after deploying the ejection charge. After preparation, the rocket was launched twice with each fincan on February 7th, 2026.

3.33 Safety

Launching rockets using I140 rocket motors requires several safety precautions before and after the event. When assembling the rocket, gloves were worn as protection against epoxy, and preparation was conducted in a ventilated and well-lit environment. Before the two launches, an

L1 certification was required for launching motors with an impulse of 320.01 Newton-seconds, which includes all H-class motors or higher. The L1 certification is a safety license that demonstrates a person's ability to safely fly and recover a rocket using an H or I-class motor. On November 8th, 2025, I prepared, launched, and received my junior L1 certification to gain the ability to fly larger rocket motors like the I140. Before launch day, motors were safely stored in a room-temperature environment to prevent any malfunctions on and before launching. On launch day, spectators had to stand 31m away from the launch pad before launch, and a five-second countdown was enforced to warn spectators of the upcoming launch. Rockets were launched at Richard Bong State Recreation Area as a part of the Tripoli Wisconsin Association's monthly launch. The launch site featured a 3048m standing waiver for all rocket launches that specific day. The rockets were only launched at wind speeds less than 32km/h (National Association of Rocketry, 2012). After launching both rockets, both motors were disposed of by burying them in the ground and lighting them on fire to get rid of any unused propellant, and the remaining liner was disposed of in the trash. Following these safety precautions ensured a safe environment for launches and assembly.

4. Results

4.1 Overview

Data from both XFOIL simulations, OpenRocket design, and experimental launches on TwinFins are covered in this section. All four graphs from XFOIL for each of the seven airfoils were plotted and compared with each other to determine the best-performing and most consistent airfoil. XFOIL's data, as well as OpenRocket simulations, were also used to predict altitude for both rocket launches on TwinFins. After graphing and comparing data from XFOIL, both qualitative observations, such as flight path and roll rate, and quantitative data from the rocket's altimeters, will be discussed, and using data, calculations on different metrics, such as stability and drag efficiency, will be done to compare both launches. After analyzing both parts, data from both the simulation side of the procedure and the experimental side of the procedure will be compared. Interpretation of these results will be presented in Section 5.

4.2 Results from XFOIL and OpenRocket

4.21 XFOIL Results

All seven airfoils were tested based on four polars to calculate stability and drag performance, and consistency. The first graph tested the coefficient of drag based on Reynolds' number for each airfoil, graphed in Fig. 15 and displayed as a table format in Table 4. Despite all airfoils exhibiting similar gradually decreasing drag profiles for the first two Reynolds' number intervals, the hexagonal flat-plate airfoil exhibits much higher drag above 0.009 C_d at the higher three intervals, while the other six airfoils exhibit significantly lower values than the hexagonal airfoil at the last three intervals, at below 0.011 coefficient of drag. These consolidated plots provide a direct correlation to viscous drag behavior at different speeds during a flight for all airfoil candidates.

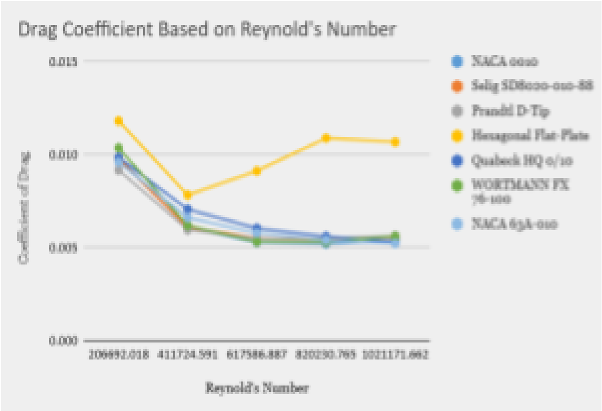

Fig. 15. Graph of drag coefficient based on Reynolds' number.

Table 4. Drag coefficient based on Reynolds' number for the seven tested airfoils from XFOIL.

	Reynold's Number				
Airfoil Name	206,692	411,724	687,586	820,230	1,021,171
NACA 0010	0.000982	0.0061	0.00529	0.00521	0.00538
SD8020-010-88	0.00977	0.0061	0.00552	0.00545	0.00556
Prandtl D-Tip	0.00917	0.00596	0.00519	0.0055	0.00561
Hexagonal Flat-Plate	0.01181	0.00785	0.00912	0.01089	0.01068
Quabeck HQ 0/10	0.00985	0.00706	0.00604	0.0056	0.00534
WORTMANN FX 76-100	0.01036	0.00619	0.00532	0.00531	0.00561
NACA 63A-010	0.00959	0.00661	0.00579	0.00541	0.00523

The second graph tested the transition point for each airfoil based on the same 5 Reynolds' number intervals, as shown in Fig. 16 and Table 5. This polar is necessary to determine the amount of skin friction drag created as a result of the airfoil's pressure distribution and transition behavior. It also displays the behavior of the airfoil's flow and how laminar or turbulent the airfoil is, and how this value decreases based on Reynolds' number. Similar to the previous graph, all seven airfoils exhibited similar gradual decreasing transition point values for the first two Reynolds' number intervals. However, the hexagonal flat-plate airfoil's transition point falls drastically at the three subsequent intervals to a transition point well below half of the chord, while the other six airfoils exhibit similar transition point behavior above a transition point of 60% of the chord throughout the entire graph.

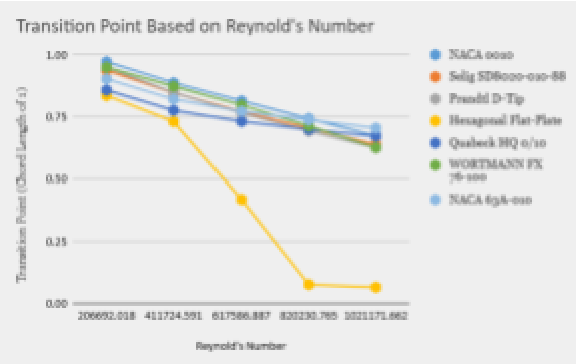

Fig. 16. Graph of transition point based on Reynolds' number.

Table 5. Transition point based on Reynolds' number.

[redacted]	Reynold's Number				
Airfoil Name	206,692	411,724	687,586	820,230	1,021,171
NACA 0010	0.9712	0.8868	0.8139	0.7427	0.6728
SD8020-010-88	0.9376	0.847	0.7713	0.704	0.6376
Prandtl D-Tip	0.949	0.8476	0.7652	0.6925	0.6252
Hexagonal Flat-Plate	0.8358	0.7311	0.4184	0.0764	0.0653
Quabeck HQ 0/10	0.8576	0.776	0.7313	0.699	0.6716
WORTMANN FX 76-100	0.949	0.8729	0.7974	0.713	0.626
NACA 63A-010	0.9022	0.8206	0.7729	0.7368	0.7045

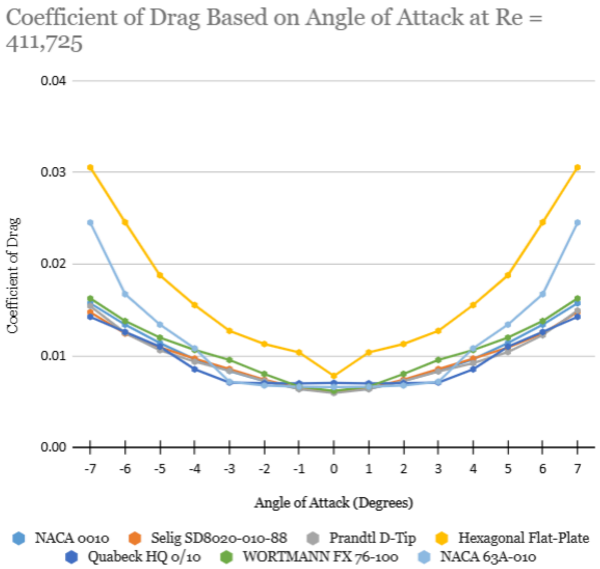

Fig. 17. Graph of drag coefficient based on angle of attack at middle-range Reynold's number of 411,725.

The third polar plotted the drag coefficient over an angle of attack range between -7 and 7 degrees at each Reynolds number interval, and this was to measure how sensitive an airfoil is when experiencing minor tilt deviations during flight. Finally, the last two plots tested both the C_d and the C_l at varying angles of attack at the constant Reynolds' and Mach numbers of 411724.591 and Mach 0.2. The tested angle of attack range was between -7° and 7°; the range was this small due to rockets experiencing very small deviations of tilt during flight. This statement was further backed by flight data from both flights in Section 4.3. The second Reynolds number interval at Mach 0.2 used for the first two graphs was selected for the last two graphs, as it lies squarely within the operating range of the TwinFins rocket during the burn and coast phases of flight, and it completely ensures no compressibility effects are present, despite compressibility effects already being negligible and corrected on all intervals. As seen in Fig. 17, which showcases the comparison between drag and tilt angle, all airfoils formed a drag bucket with the varying angles of attack. The seven airfoils at angles of attack less than $\left|5^{\circ}\right|$ exhibited similar drag behavior, with the hexagonal airfoil producing slightly more drag on average compared to the rest. At further angles of attack $\left|5^{\circ}\right|$, both the hexagonal airfoil and the NACA 63A-010 experienced higher amounts of drag, showcasing their sensitivity to drag at these higher tilt angles. Fig. 18 showcases the relationship between angle of attack and the lift coefficient, which is known as the restoration force. All 7 airfoils displayed an S-shaped lift curve, with the hexagonal flat-plate airfoil outputting the least amount of drag on average, and the other 6 airfoils outputting similar results throughout the range.

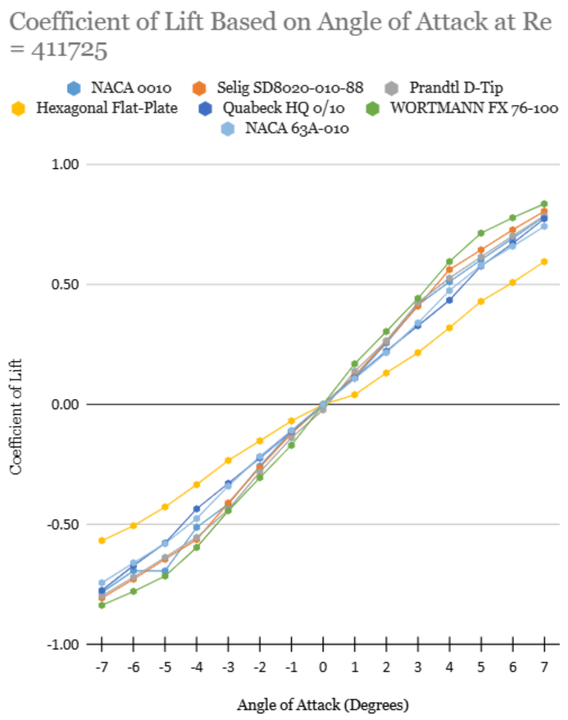

Fig. 18. Graph of lift coefficient based on angle of attack at middle-range Reynold’s number of 411,725.

4.22 OpenRocket Results

OpenRocket simulations were conducted to model the rocket used for the experimental flights, TwinFins, stability metrics, aerodynamic variables, and physical attributes. OpenRocket simulated the generic geometry of TwinFins without a specified airfoil due to the software’s constraints. Table 6 is showcases individually simulated metrics, including maximum velocity, apogee, maximum acceleration, Max-Q, and time to Apogee. Using these individual metrics, altitude, velocity, angle of attack, and dynamic pressure were plotted over time, as seen in Fig. 19. These four graphs were plotted with flight events such as motor ignition, motor burnout, apogee, parachute deployment, and ground contact. Dynamic pressure is seen to peak at the same point as the maximum velocity peaks, both at motor burnout. Altitude continues to increase at a slower rate after burnout, peaking right before velocity hits 0 at the apogee. Finally, the angle of attack is held constantly below 5° throughout the entire flight, increasing before Apogee, when velocity is under 10m/s or Mach 0.03. These graphs were created as a reference for the actual flights tested using TwinFins.

Table 6. Simulated Performance Metrics in OpenRocket

Simulated Metric	**Values**
Maximum Velocity	192 m/s
Maximum Acceleration	120 m/s^2
Max-Q	22.11 kPa
Apogee	1080 m
Time to Apogee	13.7 s

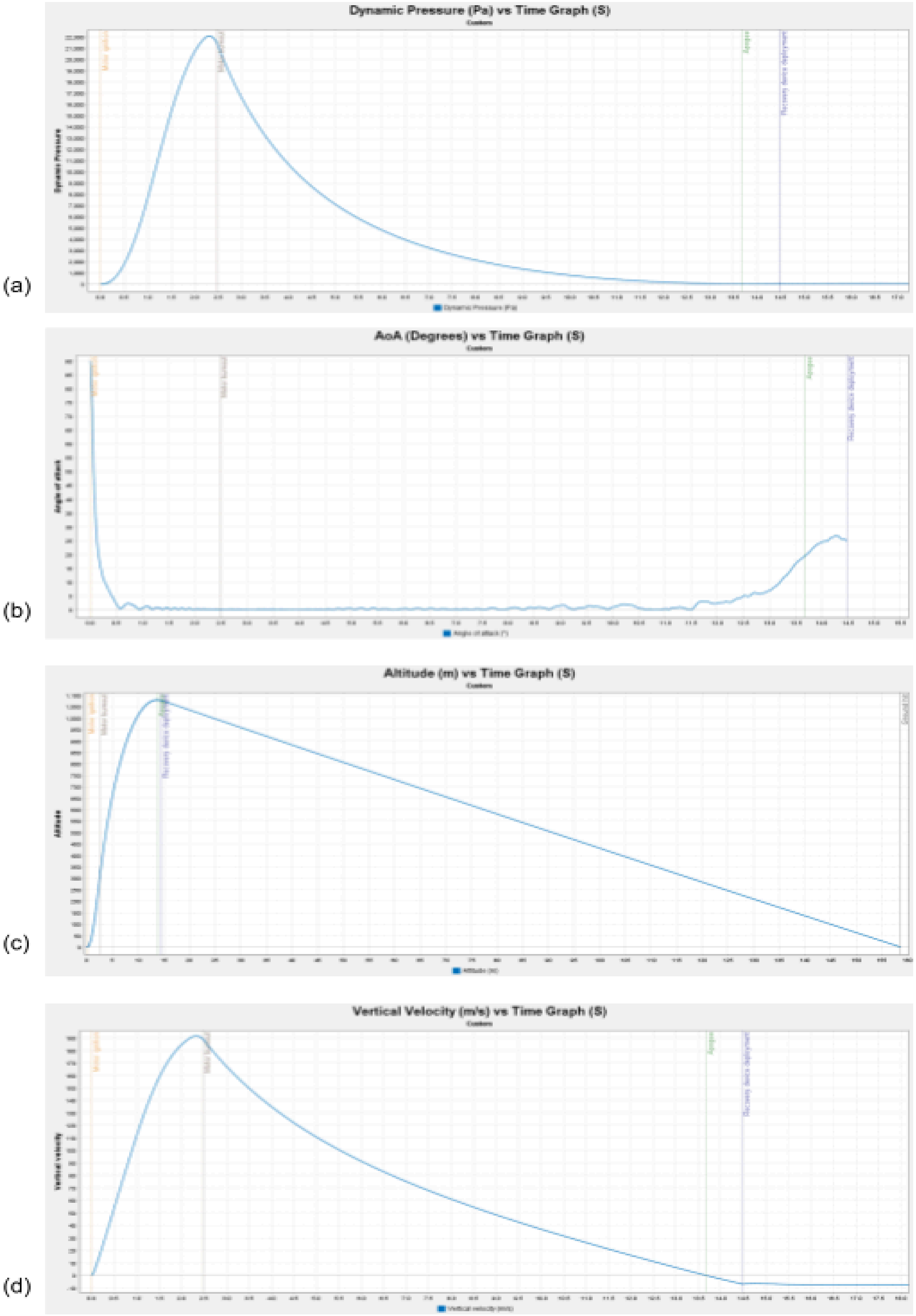

Fig. 19. OpenRocket simulated data. (a) dynamic pressure vs time, (b) AoA vs time, (c) altitude vs time, (d) velocity vs time.

4.3 Results from Experimental Launches

As mentioned previously, the experimental rocket, TwinFins, was launched twice using the specifications aside from the airfoil type. The first launch utilized the NACA 63A-010 airfoil, while the second launch utilized the hexagonal flat-plate airfoils. Due to cold weather and wiring issues on launch day, the backup EasyMini altimeter had to be excluded from both launches. As a result, all data was collected and used by the BlueRaven altimeter. Data points for the 3-axis sensors were output at 500Hz, and at 50Hz for the barometer and temperature sensor. Table 7 displays the raw flight data gathered from the BlueRaven, and Fig. 20 consists of graphs based on barometer, accelerometer, and gyro sensor recordings at the specified Hz intervals, with the blue graphs depicting the NACA 63A-010 airfoil, and the red graphs depicting the hexagonal flat-plate airfoil. Fig. 20a and Fig. 20b graph altitude over time to calculate values such as velocity and apogee, flight time, and other motion-based values. Fig. 20c and Fig. 20d graphed vertical velocity over time, based on the displacement vs time graphs. The velocity-time graphs helped calculate values such as dynamic pressure during flight. Dynamic pressure vs time graphs were depicted in Fig. 20e and Fig. 20f, and these graphs allowed for the calculation of the Max-Q, which is the point during flight where a rocket experiences the most aerodynamic stress. Both graphs calculated values until apogee. Finally, Fig. 20g and Fig. 20h were graphs showcasing the angle of attack over time during flight until burnout.

Table 7. Performance metrics from TwinFins' flights.

Metric	NACA 63A-010	Hexagonal Flat-Plate
Maximum Velocity	176.94 m/s	172.35 m/s
Max-Q	16.63 kPa	16.93 kPa
Apogee	1147.82 m	1050.04 m
Time to Apogee	13.88 s	12.78 s
Max Tilt	20.7°	4.2°

Using the raw data, five derived metrics, as mentioned in Section 3.21, were computed to provide a complete flight characterization regarding drag and stability for both airfoil configurations. Table 8 provides all 4 metrics. These four values helped gain data regarding the

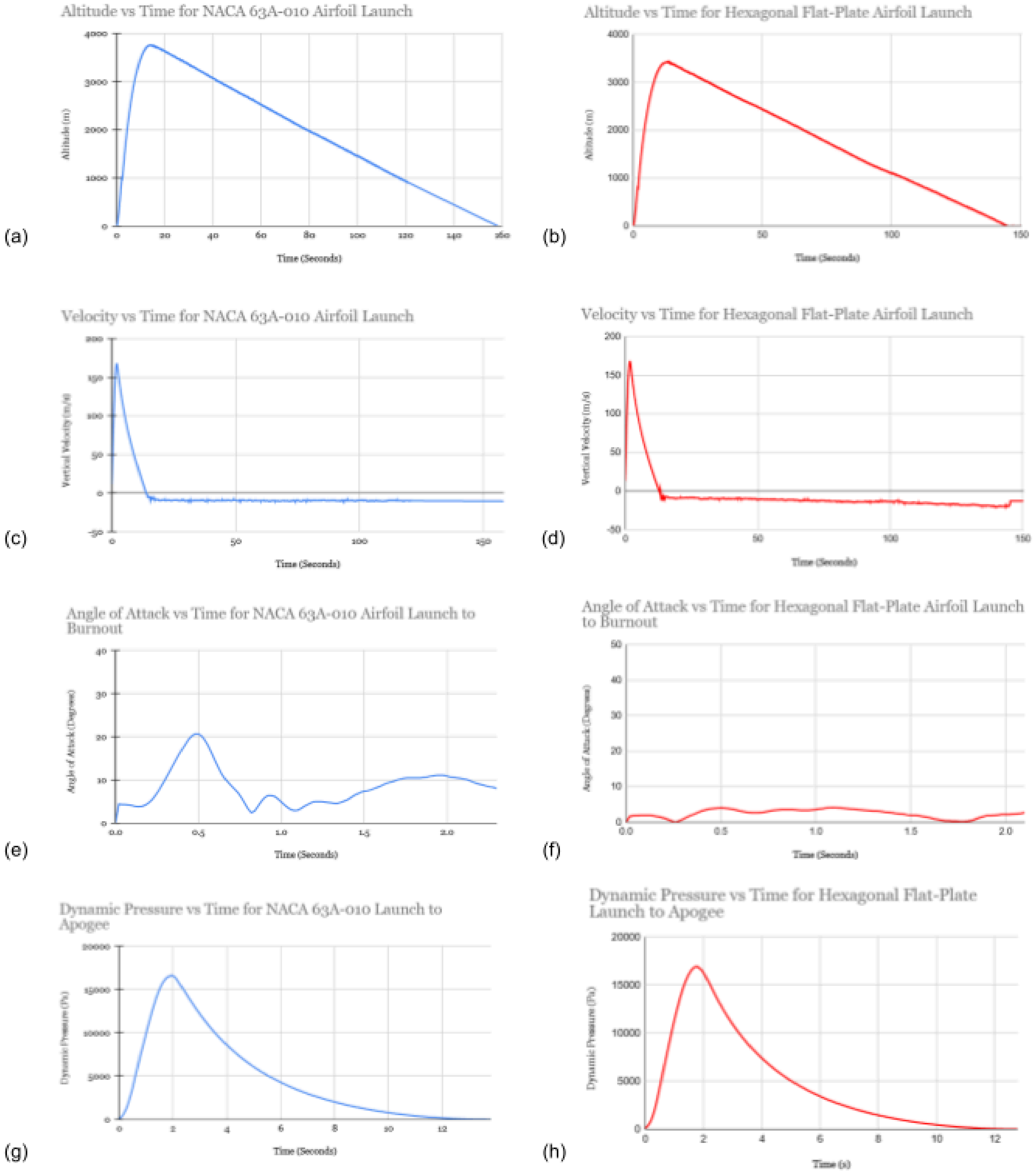

Fig. 20. Graphs from experimental rocket launches. (a) NACA 63A-010 altitude vs time, (b) flat-plate altitude vs time, (c) NACA 63A-010 velocity vs time, (d) flat-plate velocity vs time, (e) NACA 63A-010 AoA vs time to burnout , (f) flat-plate AoA vs time to burnout, (g) NACA 63A-010 dynamic pressure vs time to apogee, (h) flat-plate dynamic pressure vs time to apogee.

efficiency of the fins before and after burnout, energy efficiency, and average tilt values experienced during flight.

Table 8. Calculated metrics from launch data.

	NACA 63A-010	Hexagonal Flat-Plate
Velocity Decay Rate at Burnout	-13.4m/s	-14.3m/s
Effective Drag Coefficient	0.33	0.35
Altitude per Impulse	26.9ft per Ns	24.6ft per Ns
RMS Tilt	7.9°	2.6°

Qualitative observations were also made before and after both flights. Despite the higher complexity of the NACA 63A-010 airfoil compared to the hexagonal flat-plate airfoil, both prints took the same amount of time to complete. Additionally, both fincans received little to no damage from aerodynamic forces and ground impact after each flight.

5. Discussion

The combined simulation and flight results show a consistent, measurable tradeoff between coast-phase drag efficiency and boost-phase attitude stability for the two fin geometries tested. XFOIL and Reynolds-sweep data indicate that the hexagonal flat-plate fin exhibits higher viscous sensitivity: at a Reynolds number of approximately 10^6, the hexagonal fin's drag coefficient is 0.00783 compared with 0.00661 for the NACA 63A-010, and the hexagonal fin's transition point collapses from 0.7311 to 0.4184 and then to 0.0764 as the Reynolds number increases. At the same time, the NACA 63A-010 maintains transition points between 0.82 and 0.7 across the same sweep. These XFOIL results explain why the NACA fin produces lower drag during coast and why the hexagonal airfoil's boundary layer becomes turbulent earlier and more abruptly at higher Reynolds numbers.

Flight-scale metrics confirm the aerodynamic picture. Experimental flights recorded by the BlueRaven show the NACA 63A-010 achieved higher apogee (1147.82 m), higher peak velocity (176.94 m/s), and longer time to apogee (13.88 s) than the hexagonal flat-plate (1050.01 m, 172.53 m/s, 12.78 s). Derived metrics quantify the performance gap: effective drag coefficient is 0.33 for NACA versus 0.35 for hex, and altitude per impulse is 8.2 m/Ns for NACA versus 7.5 m/Ns for hex. These values indicate that the NACA fins convert motor impulse into altitude more efficiently and sustain coasting velocity better than the hexagonal fins.

During powered flight, the hex configuration produced lower RMS tilt from ignition to burnout (2.6°), while the NACA configuration produced higher RMS tilt (7.9° ignition→burnout). The raw flight table also reports maximum tilt values of 4.2° for hex and 20.7° for NACA. In short, the hexagonal fins provide a steadier boost phase at the cost of higher coast drag; the NACA fins reduce coast drag and raise apogee but are more sensitive to attitude excursions during boost. However, these deviations were observed due to motor chuffing occurring at the beginning of the flight. This phenomenon occurs when the motor has an uneven burn profile as it exits the launchpad, causing severe tilt angles at the beginning of flight. Despite the momentary flaw at the beginning of flight, the NACA 63A-010 airfoils showcased strong restoration forces, further backed up through the Cl vs AoA graph in XFOIL, and this phenomenon helped bring the rocket back to 0° angle of attack during flight. Future testing should involve more flights and analysis to solidify this phenomenon.

The OpenRocket simulation provides a useful reference case: simulated maximum velocity 192 m/s, maximum acceleration 120 m/s², Max‑Q 22.11 kPa, and apogee 1080 m, with a time to apogee of 13.7 s. The experimental NACA airfoil flight exceeded the simulated apogee and approached the simulated time to apogee, reinforcing that the NACA geometry's lower coast-phase drag materially improved altitude in practice.

The tradeoffs observed at model‑rocket scale map directly to many UAV and RATO (rocket‑assisted takeoff) applications. In many high‑thrust assisted launches, designers will prioritize two main characteristics: maximum velocity and apogee. Flat-plate airfoils are used widely on these systems due to their lack of complexity to manufacture and simplicity to integrate. However, these two characteristics can be further optimized through the usage of laminar airfoils, as seen through the testing. For endurance‑oriented UAVs or high‑altitude sounding platforms, where cruise efficiency and range are primary, the 63A-010 fins' lower coast-phase drag and higher altitude per impulse translate into longer range and reduced fuel/battery consumption. The measured differences, roughly 8% improvement in altitude per impulse for the laminar airfoil, are significant when scaled to repeated launches, high-cadence operations, and higher altitude missions.

Advances in additive manufacturing provide the ability to utilize more complex airfoil planforms that reduce both pressure and skin-friction drag, without having a massive tradeoff in cost and manufacturing time. When printing both sets of fincans, both the hexagonal flat-plate and the 63A-010 fincans both took 12 hours to print, and both experienced no damage from flight. Previous subtractive manufacturing and welding methods hindered the opportunity to create these advanced shapes, prompting the creation of simpler flat-plate airfoils, but with novel additive manufacturing methods, these complex airfoil shapes can be replicated with similar strength and manufacturing time, prompting their use even more.

From a sustainability perspective, the NACA geometry's higher altitude per impulse implies lower propellant requirements per mission, which translates into reduced emissions for spacecraft that use this technology. For commercial vehicles and high-cadence launch operations, even single-digit percentage improvements in drag efficiency can yield meaningful reductions in fuel consumption and environmental impact.

To bring greater credibility to the results, inaccuracies need to be addressed for future testing. The effective drag coefficients were inferred from coast-phase deceleration assuming a quadratic drag model and representative atmospheric density. Uncertainties in burnout mass, sensor alignment, and atmospheric variability affect absolute Cd values. XFOIL and OpenRocket are two-dimensional, quasi-steady tools and cannot capture three-dimensional, unsteady phenomena such as fin-root separation, vortex shedding, or transient motor misalignment. Issues regarding the motor's inconsistent burn profile for the beginning of the 63A-010 launch, also known as motor chuffing, affected RMS tilt values. Finally, despite vigorous sanding of the fincans, 3D printed profiles have layer lines that impact laminar flow on airfoils, even with small imperfections.

To reduce uncertainty and refine the trade-offs identified in this study, follow-up work should combine higher-fidelity aerodynamic testing with controlled-flight experiments and careful mass‑property characterization. Utilization of CFD or wind‑tunnel testing of the two fin geometries will resolve limitations held by two-dimensional simulators, validate transition behavior, and produce highly accurate drag coefficient estimates that account for fin‑root, turbulent flow, and vortex shedding effects. Including more launch tests under the same environmental conditions will reinforce conclusions and expose variability in flight, such as motor chuffing, unexpected wind gusts, etc. Comparison of differently post-processed fin cans after 3D printing will determine to what extent laminar flow airfoils are affected by imperfections. This testing will help determine the best way to mitigate additive manufacturing imperfections. Finally, for UAV and RATO applications, incorporate the measured RMS tilt and Cd differences into system‑level simulations to evaluate mission‑level tradeoffs (range, payload, and launch robustness) and prioritize design changes that deliver the largest operational benefit.

6. Conclusion

The experimental and simulation evidence demonstrates a clear answer: Despite the traditional favorable qualities that hexagonal flat-plate airfoils have to offer, such as their high strength and simple manufacturability, with novel additive manufacturing technologies, NACA 63A‑010 fins deliver superior drag efficiency and higher altitude per impulse without a detrimental loss in strength and manufacturing time. Quantitatively, the NACA configuration produced higher apogee (1147.82 m vs 1050.01 m), lower effective drag (0.33 vs 0.35), and higher altitude per impulse (8.2 m/N·s vs 7.5 m/N·s) compared to hexagonal flat-plate airfoil. These differences are large enough to influence fin selection for both experimental rocketry and practical aerospace applications.

For UAVs and RATO systems, the choice is mission dependent: select hex‑like, robust geometries when launch robustness is critical; select NACA‑style, low‑drag geometries when cruise efficiency, range, and altitude are primary. Additive manufacturing and surface engineering now make it feasible to pursue hybrid solutions that combine the robustness of simpler platforms with the cost efficiency of streamlined airfoils.

Implementing the recommended follow‑up testing and manufacturing experiments will reduce uncertainty, validate findings, refine the quantified tradeoffs, and enable fin designs that better balance performance, manufacturability, and sustainability. The results here inform both small‑scale experimental rocketry and broader aerospace efforts where drag reduction, launch reliability, and environmental impact are increasingly central design drivers.

Acknowledgements

I would like to thank Mrs. Jann Hawkins for her continued support throughout the course of this project, as her check-ins and document revisions have been more than insightful to my project. I would also like to thank the Illinois Stem Society and ScienceCoach for their continued help and support for material purchases and logistics handling. Additionally, I want to thank Marty Bathgate (BS, MS) for their continuous support throughout the project, including help regarding simulation software such as XFLR5, enlightenment on airfoil-related theory, project meetings, and paper revisions. Finally, thank you to Benjamin Quach for his help regarding paper revision, simulation assistance, and project strategy, as well as Sid Nagarajan (BS) for his additional project assistance and procedure guidance. I am very thankful to everyone mentioned, as this individual project was made a team effort due to small contributions from these influential mentors. I hope to carry the learnings gained from this project to guide me on my future career path in aerospace engineering, in college, and in life.

References

[AIAA conference paper 2025‑98103]. AIAA SciTech Forum. https://arc.aiaa.org/doi/epdf/10.2514/6.2025-98103

Airfoil Tools. (n.d.). Airfoil Tools. http://airfoiltools.com/index

Altus Metrum. (n.d.). EasyMini user guide. https://altusmetrum.org/AltOS/doc/easymini.html#_hooking_up_batteries

Anderson, D. F., & Eberhardt, S. (2001). Understanding flight. McGraw-Hill.

Anderson, J. D. (2016). Introduction to flight (8th ed.). McGraw-Hill Education.

Anderson, J. D. (2017). Fundamentals of aerodynamics (6th ed.). McGraw-Hill Education.

BSR. (n.d.). Sustainability in space: The next frontier. Business for Social Responsibility. https://www.bsr.org/en/emerging-issues/sustainability-in-space-the-next-frontier

Drela, M. (1989). XFOIL 6.9 user guide. Massachusetts Institute of Technology. https://web.mit.edu/drela/Public/papers/xfoil_sv.pdf

Featherweight Altimeters. (2025, September 10). Blue Raven user's manual. https://www.featherweightaltimeters.com/uploads/1/0/9/5/109510427/blue_raven_users_manual_2025_sept_10.pdf

Federal Aviation Administration. (2016). Pilot's handbook of aeronautical knowledge (FAA-H-8083-25B). U.S. Department of Transportation.

Leishmann, J. (2022.). Turbulent flows. In Introduction to Aerospace Flight Vehicles. Embry-Riddle Aeronautical University. https://eaglepubs.erau.edu/introductiontoaerospaceflightvehicles/chapter/turbulent-flows/

National Aeronautics and Space Administration. (1993). [Mean aerodynamic chord formulation] (NASA Technical Memorandum 19930091829). https://ntrs.nasa.gov/api/citations/19930091829/downloads/19930091829.pdf

National Aeronautics and Space Administration. (2022). What is drag? NASA Glenn Research Center. https://www1.grc.nasa.gov/beginners-guide-to-aeronautics/what-is-drag/

National Aeronautics and Space Administration. (n.d.). 3D-printed rocket launched using innovative NASA alloy. NASA Marshall Space Flight Center. https://www.nasa.gov/centers-and-facilities/marshall/3d-printed-rocket-launched-using-innovative-nasa-alloy/

National Aeronautics and Space Administration. (n.d.). Learn about aerodynamics. NASA Glenn Research Center. https://www1.grc.nasa.gov/beginners-guide-to-aeronautics/learn-about-aerodynamics/

National Aeronautics and Space Administration. (n.d.). Viscosity and Sutherland's law. NASA Glenn Research Center. https://www.grc.nasa.gov/www/BGH/viscosity.html

National Oceanic and Atmospheric Administration, National Aeronautics and Space Administration, & U.S. Air Force. (1976). U.S. standard atmosphere, 1976 (NOAA-S/T 76-1562). https://www.ngdc.noaa.gov/stp/space-weather/online-publications/miscellaneous/us-standard-atmosphere-1976/us-standard-atmosphere_st76-1562_noaa.pdf

Niskanen, S. (2013). OpenRocket: An open source model rocket simulation software (Master's thesis). Aalto University. https://openrocket.sourceforge.net/thesis.pdf

Sandia National Laboratories. (2024, January 25). Changing the world one dimple at a time. Sandia LabNews. https://www.sandia.gov/labnews/2024/01/25/changing-the-world-one-dimple-at-a-time/

Wassgren, C. (n.d.). Notes on thermodynamics, fluid mechanics and gas dynamics. Purdue University. https://engineering.purdue.edu/~wassgren/notes/NotesOnThermodynamicsFluidMechanicsAndGasDynamics_Wassgren.pdf